

Opto-Electrochemical Synaptic Memory in Supramolecularly Engineered Janus 2D MoS₂

Ye Wang, Bin Han, Marcel Mayor, and Paolo Samorì*

Artificial synapses combining multiple yet independent signal processing strategies in a single device are key enabler to achieve high-density of integration, energy efficiency, and fast data manipulation in brain-like computing. By taming functional complexity, the use of hybrids comprising multiple materials as active components in synaptic devices represents a powerful route to encode both short-term potentiation (STP) and long-term potentiation (LTP) in synaptic circuitries. To meet such a grand challenge, herein a novel Janus 2D material is developed by dressing asymmetrically the two surfaces of 2D molybdenum disulfide (MoS₂) with an electrochemically-switchable ferrocene (Fc)/ ferrocenium (Fc⁺) redox couple and an optically-responsive photochromic azobenzene (Azo). Upon varying the magnitude of the electrochemical stimulus, it is possible to steer the transition between STP and LTP, thereby either triggering electrochemical doping of Fc/Fc⁺ pair on MoS₂ or controlling an adsorption/desorption process of such redox species on MoS₂. In addition, a lower magnitude LTP is recorded by activating the photoisomerization of azobenzene chemisorbed molecules and therefore modulating the dipole-induced doping of the 2D semiconductor. Significantly, the interplay of electrochemical and optical stimuli makes it possible to construct artificial synapses where LTP can be boosted to 4-bit (16 memory states) while simultaneously functioning as STP.

among neurons. Synaptic plasticity represents the capacity of synapses to weaken or strengthen over time, as a response to decreases or increases in their activity.^[1] To simulate synaptic plasticity, artificial synaptic devices are ideal elements to mimic synaptic learning rules in the human brain by incorporating memory functions with both short-term potentiation (STP) and long-term potentiation (LTP). These devices play an important role in future emerging technologies such as artificial brain, neuromorphic computing, and big data. Plasticity in electronic devices can be expressed either by reversibly modifying the intrinsic physical properties of the active material such as ferroelectricity, vacancy migration, and phase changing, or by modulating the interface of different materials in the electronic device such as electrochemical memory formed by metal filament and charge trapping at semiconductor/dielectric interface.^[2]

Synaptic devices are commonly made of silicon, oxides, and organic compounds.^[3] Recently, 2D materials have also been incorporated as active components in artificial synapses by taking advantage of the unique memory formation mechanisms resulting from their distinct physical and chemical properties.^[4] In particular, their atomic thickness and large surface-to-volume ratio render them particularly sensitive to interactions with any chemical species present in the environment. Their ultraflat surfaces enable the generation of atomically controlled interfaces in which the 2D materials can interact with molecules or functional nanostructures via dipole–dipole forces or charge transfer, thereby tuning the opto-electronic properties of the active 2D material.^[5] When integrated in electrical devices, this interfacial tuning and the emergence of novel properties offer a powerful means to realize artificial synapses. For semimetallic 2D materials such as graphene, the conductivity modulation via charge transfer is typically limited within one order of magnitude.^[6] For insulating 2D materials like hexagonal boron nitride (h-BN), as a result of the abrupt conductivity changes mediated by charge trapping at defect states, it is difficult to produce multiple synaptic levels.^[7] Conversely, semiconducting 2D materials such as transition metal dichalcogenides meet the requirements of broad conductivity tuning with multilevel synaptic manipulations.^[8] Charge carrier density changes that are modulated by external stimuli (e.g., electricity, light, etc.) can be recorded


1. Introduction

Artificial synapses mimic the synaptic behavior in nerve cells which relies on the transmission of electrical or chemical signals

Y. Wang, B. Han, P. Samorì
University of Strasbourg
CNRS
ISIS UMR 7006, 8 Allée Gaspard Monge, Strasbourg F-67000, France
E-mail: samori@unistra.fr

M. Mayor
Department of Chemistry
University of Basel
St. Johannisring 19, Basel 4056, Switzerland

M. Mayor
Karlsruhe Institute of Technology KIT
Institute for Nanotechnology
P.O. Box 3640, 76021 Karlsruhe, Germany

 The ORCID identification number(s) for the author(s) of this article can be found under <https://doi.org/10.1002/adma.202307359>

© 2023 The Authors. Advanced Materials published by Wiley-VCH GmbH. This is an open access article under the terms of the Creative Commons Attribution License, which permits use, distribution and reproduction in any medium, provided the original work is properly cited.

DOI: 10.1002/adma.202307359

electrically thus mimicking the process of neuron's STP and LTP.^[9]

One strategy to realize 2D semiconductor-based artificial synapses consists in exerting dynamic modulation of carrier density. Common approaches involve electrostatic doping through the gate electrode modulation, or via electrochemical metalization through a DC voltage control.^[10] These methods could mimic either STP or LTP in an artificial synapse. However, the combination of both function's expression within a single synaptic device still represents a grand challenge. In fact, hitherto the development of artificial devices emulating the synaptic functions of both STP and LTP characteristics requires additional separate electronic circuitries, hence it does not represent an energy-efficient computing solution for artificial intelligence. Therefore, devising novel mechanisms for bio-mimetic devices that fulfill the requirement of multiple logic operations such as mimicking both STP and LTP is highly sought after.

By mastering the more-than-Moore approach relying on functional diversification, a viable solution to impart additional functionalities to 2D semiconductors consists in their interfacing with chemical species enabling both STP and LTP in an artificial synapse.^[9] The successful functionalization requires simultaneously: 1) the generation of electrical signal in the 2D semiconductor under stimuli; 2) for STP operation, the electrical signal should vanish just after having removed the external stimulus; 3) for LTP operation, the electrical signal should be retained after the removal of the stimulus; 4) the functionalities should enable to emulate multiple synaptic levels; 5) the functionalities exploited should be compatible with 2D materials and should be robust upon application of the external stimuli. Organic molecules are appropriate components to meet all these requirements since their electrical and chemical properties can be remote-controlled by means of external stimuli such as electrochemical, electromagnetic, or electrical fields. For example, electrons can be released or captured from redox couples through charge transfer when applying electrochemical stimuli to the system whereas photochromic molecules can be toggled between different isomeric forms as a response to optical stimuli. The combination of such two kinds of stimuli-responsiveness (to electrochemical and optical stimuli) when interfaced to 2D semiconductors can enable the versatile manipulation of 2D artificial synapses.

In this work, we have devised a 2D semiconductor-based artificial synapse by exploiting their asymmetric molecular functionalization with redox and light-responsive molecular systems. As an archetypical 2D semiconductor, we have employed a few-layer thick 2H-molybdenum disulfide (MoS_2), behaving as a synaptic signal receptor and amplifier material. The existence of well-defined faces in 2D MoS_2 makes it possible to expose them to different local environments thereby dressing them with distinct functions, to form Janus organic/2D MoS_2 /organic stack through asymmetric functionalization.^[11] On the other hand, to meet the above-mentioned five functional features, it is essential to choose carefully 1) redox pairs that could impart both STP and LTP signals to MoS_2 by electrochemical stimuli, like ferrocene/ferrocenium (Fc/Fc^+); 2) photochromic molecules which could create dynamic charge carrier tuning in MoS_2 upon optical stimuli at different wavelengths, such as azobenzene (Azo). These molecules can be interfaced either at the covalent or non-covalent level with the basal plane of MoS_2 to form supramolec-

ular Janus Fc/MoS_2 /Azo stacks capable of emulating both STP and LTP synaptic signals with electrochemical stimuli while establishing fine multilevel LTP with optical stimuli. In addition, we found out that the application of a potential to redox molecules such as Fc does not only offer a tool to modulate their charge transfer with 2D MoS_2 but also to control their adsorption/desorption process onto the surface of the 2D material thereby mimicking an unprecedented LTP activity in artificial synapses. Our results demonstrate that the careful design of supramolecular Janus 2D materials enables the emergence of a novel class of artificial synapses for next-generation energy-efficient computing.

2. Results and Discussion

Figure 1a displays the key component of our artificial synapse, a few-layer thick (ranging from 3–6 layers in different devices) 2D MoS_2 asymmetrically functionalized on two sides of the basal plane with organic functional layers. The top surface is coated with an organometallic complex based on ferrocene (Fc) which is prone to undergo oxidation to ferrocenium (Fc^+) as a result of an electrochemical stimulus. The bottom surface is decorated with a chemisorbed self-assembled monolayer (SAM) of 4'-(biphenyl-4-ylazo)-biphenyl-4- thiol] molecule which undergoes photoisomerization between the *trans*- and the *cis*-isomer when exposed to light at specific wavelengths.^[12] This Janus-like functionalization enables the modulation of MoS_2 conductivity by means of two independent remote controls. In order to collect the electrical signals, we fabricated a vertical junction consisting of two gold electrodes (source and drain) placed on the bottom and on the top of the asymmetrically functionalized MoS_2 . Gold has been chosen as it is the ideal electrode for the tailoring of a robust SAM through the Au-S bond formation, with the latter being compatible with nanofabrication processes. The morphology of gold films before and after molecular functionalization with the chemisorbed Azo-SAM has been explored by Atomic Force Microscopy (AFM). The topographical AFM images in Figure S1 (Supporting Information) reveal that the chemisorbed Azo-SAM exhibits homogeneous and very flat morphology, as evidenced by a root-mean-square roughness (R_{RMS}) of 0.253 nm as estimated on a region of $5 \times 5 \mu\text{m}^2$. In parallel, to confer redox responsiveness through the electrochemical stimulus, we dissolved Fc in an ion gel composed of $(\text{DEME})^+(\text{TFSI})^-/\text{PVDF-HFP}$ (Figure S2, Supporting Information). The electrochemical stimulus was applied via an additional top-gate gold electrode (denoted as V_{tg}). To realize the artificial synapse, the device can operate according to 3 modes: a) STP upon applying a small magnitude electrochemical stimulus; b) LTP upon applying a large magnitude electrochemical stimulus; c) under each established LTP state, fine-tuning of sub-memory-states of LTP is realized by means of optical stimuli Figure 1b. The overall three operating modes in the Janus 2D MoS_2 denote a unique artificial synapse prototype that finally emulates both STP and multilevel LTP within an individual device.

First, we evaluate the formation of STP and LTP with electrochemical stimulus. STP and LTP are established as a result of the responsiveness of the redox Fc and Fc^+ pair to the electrochemical stimuli. As a robust electrochemical redox pair, the redox reaction of ferrocene results in a typical oxidation and reduction peak in the cyclic voltammetry (CV) curve with MoS_2 used as the work-

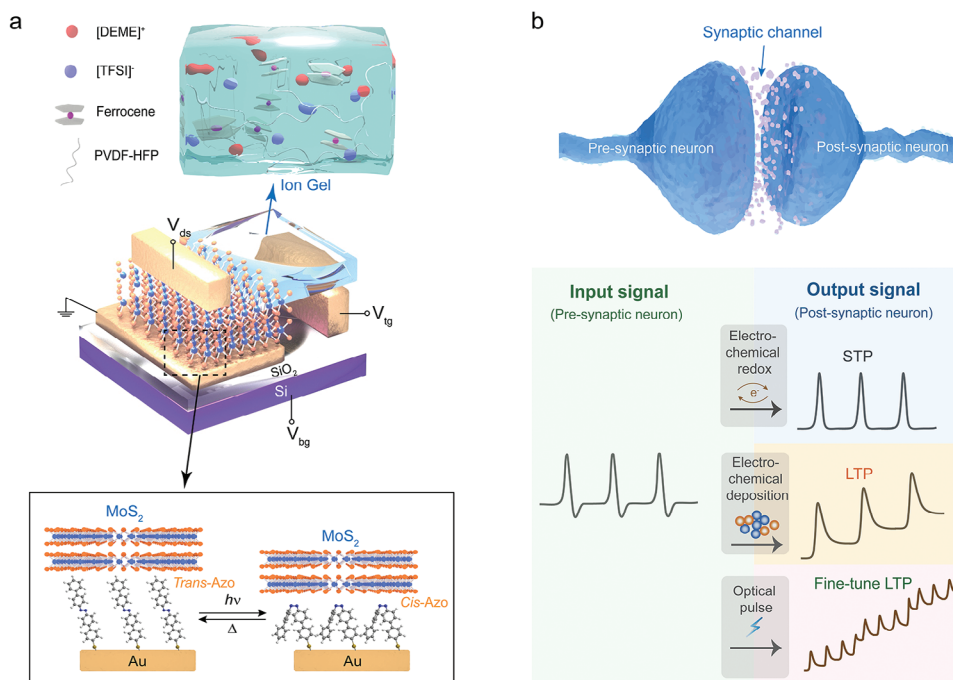


Figure 1. Working principle of synaptic Janus Fc/MoS₂/Azo. a) Schematic representation of device structure of Janus Fc/MoS₂/Azo. b) Mechanism of STP, LTP, and finely tuned LTP synaptic signal formation from Janus Fc/MoS₂/Azo by electrochemical and optical inputs with a corresponding sketch of pre- and post-synaptic neuromorphic activity.

ing electrode **Figure 2a**. Figure 2b shows that when a positive potential below +2.5 V between MoS₂ and Fc/ion gel is applied, Fc is oxidized to Fc⁺ while releasing an electron. Driven by the vertical electric field, this extra electron is immediately transferred to MoS₂. Since MoS₂ is an n-type semiconductor, with the major charge carrier being electrons, the additional electron gives rise to an increase in the electron conductivity in the 2D material. The electron transfer can be directly observed as a change in linear slope in the transfer ($I_{ds} - V_{gs}$) curve of MoS₂ (Figure S3, Supporting Information). When the potential reaches +2.5 V, as more Fc is oxidized to Fc⁺ releasing electrons to MoS₂, MoS₂ becomes heavily electron-doped, forming a strong vertical electric field across the ion gel. This electric field drives the free Fc⁺ toward MoS₂, forming a stable adsorbed layer of a molecule at the ion gel/ MoS₂ interface. As is shown in Figure 2c, with 1 mg mL⁻¹ Fc in the ion gel, a positive potential leads to a conductance of 5.24×10^{-6} S at +2 V compared to 3.32×10^{-6} S at 0 V, revealing electron transfer from Fc to MoS₂ with the ferrocene being oxidized to Fc⁺. Conversely, applying a -2 V potential results in a decrease of conductance to 1.87×10^{-6} S, indicating that MoS₂ donates electrons to Fc⁺ causing its reduction to Fc. Upon removal of the electrical bias, the conductance returns to its original value of 2.42×10^{-6} S. This indicates that a reversible charge transfer process between Fc and MoS₂ occurs when applying a ± 2 V potential window. We observe a small clockwise hysteresis which corresponds to charge trapping MoS₂/ion gel interface.^[13] The increase of the potential window to 3 V is accompanied by an expansion of the hysteresis window to 3.1 V, becoming anticlockwise. The conductance at 0 V changes from 1.82×10^{-6} S in forward scan (“SET” half-cycle in green) to 2.83×10^{-5} S in reverse scan (“RESET” half-cycle in black) and can only be erased by applying a

negative potential. In order to understand such different behavior observed upon enlarging the applied potential, we analyzed the local CV of Fc/Fc⁺ upon using MoS₂ as a working electrode Figure 2d. Typically, in a 3 V measuring window, the MoS₂/ion gel/Au junction shows a small and broad oxidation peak at +1.2 V and a reduction peak at -0.2 V. Due to the special device configuration and measurement conditions, similar observations have not yet been reported. We speculate that the (TFSI⁻) anion in the ionic liquid interacts with the sulfur vacancy in MoS₂, generating an atomically local redox environment on the surface.^[14] The unraveling of the mechanism of interaction between ionic liquid and MoS₂ will be the subject of future studies. Upon addition of ferrocene in the ion gel, at the positive potential range, we have observed a typical oxidation peak at 1.0 V. At higher positive potential, another peak at 2.5 V appears. Since Fc⁺ can hardly be further oxidized at such potential, this peak at higher potential can be interpreted as a fingerprint of the physical adsorption of Fc⁺ onto MoS₂.^[15] We suspect the origin of the additional peak being the additional current produced by the dynamic movement of free Fc⁺ ions in the ion gel toward the surface of MoS₂ without intercalating effect (Detailed discussions of molecular intercalation can be found in Figures S4–S6, Supporting Information). Upon cycling, the intensities of both the adsorption peak and the oxidation peak are found to decrease, indicating after each CV cycle, more Fc⁺ is absorbed on MoS₂ and less free Fc/Fc⁺ pairs participate in the redox reaction in the ion gel (Figure S7, Supporting Information). Similarly, the peak at +0.2 V suggests Fc⁺ can be reduced to Fc and a further desorption-related peak is observed at -1.4 V. The peak is broad and features a low current magnitude, indicating that the few adsorbed molecules are released freely into the gel, providing evidence that the desorption process

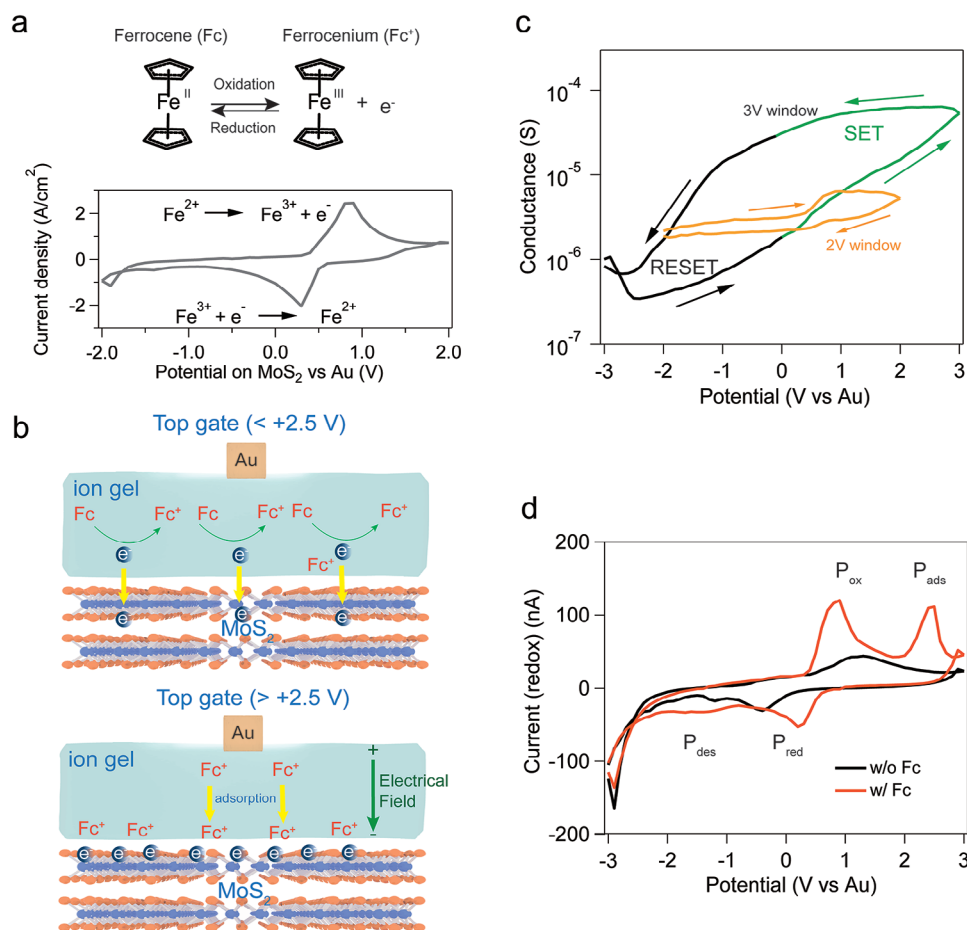


Figure 2. Analysis of STP and LTP by electrochemical stimulus. a) Chemical redox reaction of ferrocene and ferrocenium with the corresponding CV curve. b) Schematic representation of electrochemical charge transfer between ferrocene/ferrocenium and MoS₂ and adsorption of ferrocenium. c) Electrochemical hysteresis of 2D MoS₂ with ±2 and ±3 V of potential window. d) On-device cyclic voltammetry curves of ion gel (black curve) and ion gel with Fc/Fc⁺ redox pair (orange curve).

is inhomogeneous and less effective than adsorption. This means that Fc⁺ could robustly adhere on MoS₂ yielding efficient electron transfer resulting in an increased conductivity of MoS₂ even once the external potential is removed. The long-term stable conductivity modulation is ideal for non-volatile memory which functions as LTP in synaptic devices. The application of a potential exceeding +2 V allows to trigger the adsorption process, whereas upon applying a smaller bias only an instantaneous conductivity change can be induced, serving as STP in artificial synapse. By comparing to the hysteresis curves in Figure 2c, we reveal that in our particular Fc/MoS₂ hybrid system, upon tuning the potential that is applied between MoS₂ and Fc/ion gel, two distinct electrochemical states can be obtained to realize both volatile (STP, at <2 V) and non-volatile (LTP, at >2 V) memories.

Though Fc/MoS₂ could dynamically create STP and LTP with relatively fast response (i.e., on the time scale of 800 ms for both STP and LTP) and large signal-to-noise ratio ($\approx 10^3$ for STP and $\approx 10^4$ for LTP), the number of non-volatile memory levels in LTP is limited due to the abrupt conductivity change mediated by the immediate electrochemical adsorption of Fc⁺ on MoS₂. Consequently, likewise other electrochemical memristors, Fc/MoS₂ only shows 4 distinctive memory states (2 bits) which is not ad-

equate for multi-level non-volatile memory applications. To overcome this problem, we have integrated an additional functionality that could deliberately introduce sub-memory states for multi-level LTP, by embedding photochromic molecules. The latter responds to optical stimuli by reversibly changing their chemical structure, thereby modifying their coupling with molecules and materials in proximity. Their unique function has been successfully exploited for the fabrication of non-volatile optical memories when combined with organic molecules, polymers, and 2D materials.^[16] Previously, we have reported photoisomerization of chemisorbed azobenzene self-assembled monolayers could influence the work function of gold by electronic reorganization on the surface. The change on the net molecular dipole on the gold surface from 5.30 D in *trans*-Azo to 2.81 D in *cis*-Azo determines a work function increases from 5.15 eV in Au/ *trans*-Azo to 5.22 eV in Au/ *cis*-Azo junctions.^[17] The azobenzene isomerization is also accompanied by a major change in the molecular contour length, being 1.9 and 1.2 nm in the *trans*- and *cis*-isomer, respectively, which results in a significant variation in the tunneling modulated injection at the electrode-semiconductor interfaces in organic field-effect transistors, which was employed to fabricate optically responsive electronic devices.^[18] In our

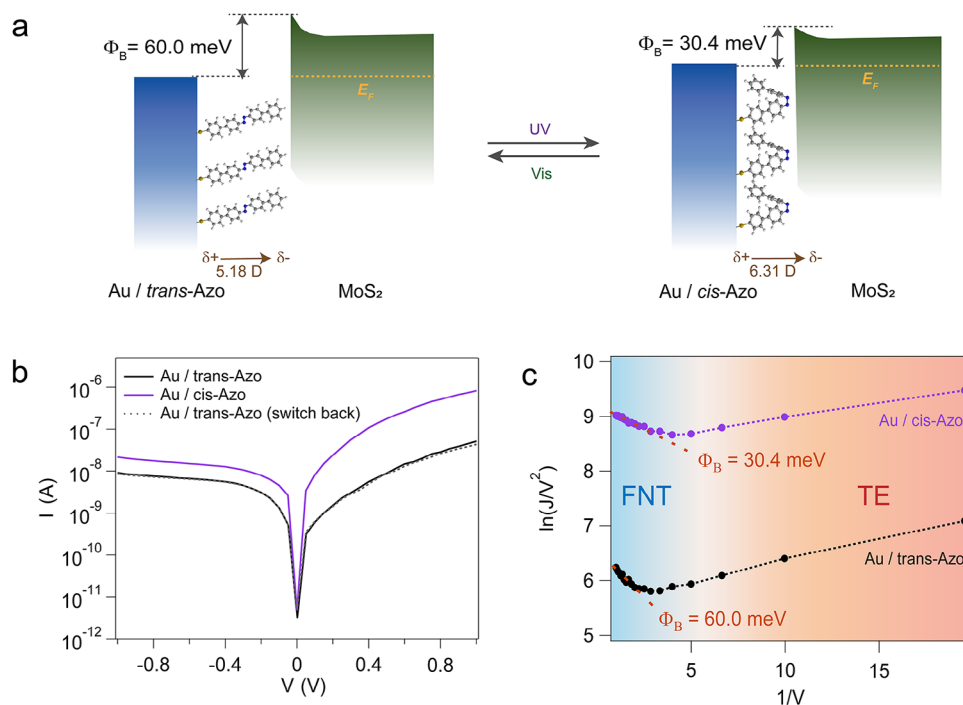


Figure 3. Analysis of fine LTP by optical stimulus. a) Band alignment of Au-Azo and MoS₂. b) Output curves of Au-Azo/MoS₂/Au under photoisomerization between *trans*- and *cis*-Azo. c) Fowler-Nordheim tunneling analysis of Au/*cis*-Azo and Au/*trans*-Azo contacts to MoS₂, showing variation of tunneling barrier height with different molecular isomerization. The linear regression fitting of FNT reports a coefficient of determination R² of 0.9994 and 0.9947 for Au/*trans*-Azo and Au/*cis*-Azo.

Au/Azo/MoS₂ hybrid system, because of the limited thickness of MoS₂ nanosheets (being 5 layers hence corresponding to <5 nm) their electronic properties could be largely influenced by the interaction with adsorbed molecules. Two can be the effects that contribute to the current response to the light stimulus in the hybrid Au/Azo/MoS₂ junction: i) The change in Azo-SAM thickness determining a tunneling governed variation in the charge transport through the junction. ii) As is sketched in Figure 3a, the Fermi level pinning at the Au-2D MoS₂ interface is characterized by a 70 meV work function change still affecting the barrier height at semiconductor-metal contact. Molecular dipoles are able to induce local gating effects on 2D materials, resulting in electrostatic doping even with small dipole changes.^[5,19] The photoisomerization of azobenzene interfacing MoS₂ could therefore shift the Fermi level of MoS₂ dynamically by dipolar doping.^[20] Moreover, the tightly-packed nature of the chemisorbed self-assembled at the interface maximizes the doping with a collective effect.^[19b,20,21] By and large, the sum of the two factors (tunneling distance, dipolar doping) associated with the *trans* to *cis* azobenzene photoisomerization enables a high-magnitude dynamic tuning of MoS₂ conductivity. Raman analysis of the same MoS₂ flake supported on Au and SiO₂ reveals nearly identical spectra, characterized by a lack of shift of both E_{12g}¹ and A_{1g} peaks (Figure S8, Supporting Information). However, when the MoS₂ nanosheet is supported on Azo-SAM chemisorbed on Au, a red shift of 2.9 cm⁻¹ for both peaks has been observed, indicating n-doping of MoS₂, in accordance with the lowering of the work function upon molecular functionalization as determined by photoelectron spectroscopy and macro-

scopic Kelvin probe measurements.^[17,18,19b] Figure 3b displays the *I*-*V* curve measured on a vertical Au/Azo/MoS₂/Au junction by sweeping the voltage from -1 V to +1 V. The asymmetry in the curves reflects the different charge injection at the two metal-semiconductor interfaces and it varies based on the isomeric state adopted by the Azo molecules. A more moderate asymmetry has been observed in such Au/Azo/MoS₂/Au junction when the Azo is in its *trans* form, with the current being on the same order of magnitude, that is, reaching 10⁻⁸ A at -1 V and +1 V. Conversely, for *cis* isomers a diode-like behavior has been recorded, with the current at +1 V being 10.4 times higher than at -1 V, whereas the Au/*cis*-Azo/Au junction, the rectification ratio displayed 2.0-fold than that of Au/*trans*-Azo/Au junction, indicating conditions for electron tunneling is changed. The photoswitching has been observed also at low temperatures at 6 K (Figure S9, Supporting Information). The transport through the Au/Azo/MoS₂/Au junction has been assessed by fitting with Fowler-Nordheim tunneling (FNT)

$$J_{FNT} \propto V^2 \exp \left[\frac{-8\pi\sqrt{2m^*}\varphi_B^{\frac{3}{2}}d}{3hqV} \right] \quad (1)$$

where *V*, *m*, *φ_B*, *d* are the bias voltage, effective electron mass, tunneling barrier, and tunneling thickness respectively. *h* stands for the Planck constant and *q* is the elementary charge. By plotting ln(*J*/*V*²) vs 1/*V*, we could obtain the Fowler-Nordheim plot Figure 3c which exhibits two regimes, the FNT and thermionic emission (TE) at high and low *V*, respectively.^[22] By extracting the

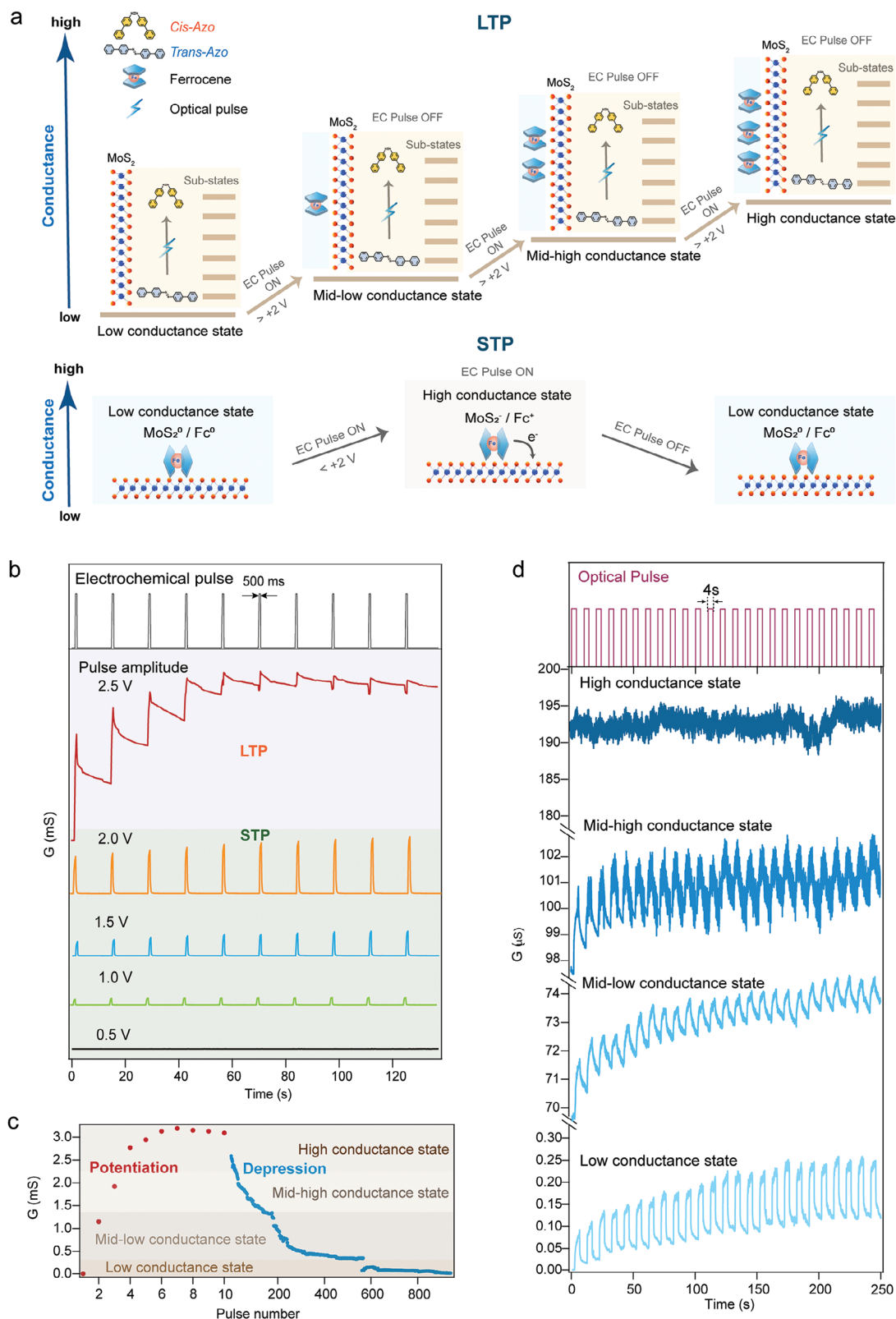


Figure 4. Multilevel STP and LTP operation by combined electrochemical and optical pulses. a) Schematic representation of conductance variation controlled by electrochemical coupled with optical memory. b) Conductance change under different electrochemical pulses showing a transition between STP and LTP when a bias >2.0 V is applied. c) Potentiation and depression cycles of electrochemical memory. The potentiation voltage is >2 V and the depression voltage is -5.0 V. d) Time-dependent multilevel LTP with major states recorded with EC pulses and sub-states achieved upon optical pulses.

slope in the FNT region, the tunneling barrier (φ_B) of Au/*trans*-Azo/MoS₂ and Au/*cis*-Azo/MoS₂ can be estimated as 60.0 and 30.4 meV, respectively. The modulation of φ_B is also found to be reversible (Figure 3b) and the conductivity change of MoS₂ can be easily controlled by tuning the molecular photoswitching dynamics, that is, illumination time, light intensity, and wavelengths without the appearance of current leakage (Figure S10, Supporting Information). The major advantage of using photochromic molecules resides in the subtle and simple manipulation of electrical output signals in the solid state, which is ideal for establishing LTP at the small discrepancy of memory levels. The back thermal switching of Azo also exhibits high *Trans*→*Cis* conversion (88%), slow kinetics (rate constant $k = 2.82 \pm 0.14 \text{ s}^{-1}$) and long lifetime (half lifetime $t = 41 \text{ min}$), being a suitable element for non-volatile memory.^[12,23] By embedding photoswitchable azobenzene at the Au/MoS₂ interface, it is possible to compensate the drawbacks associated with the absence of multi-level non-volatile memory states driven by electrochemically induced LTP, while not perturbing the memory control of Fc/Fc⁺/MoS₂.

Finally, our Janus Fc/MoS₂/Azo has been exploited to emulate an artificial synapse by enabling both STP and multi-level LTP through the joint remote control of electrochemical and optical stimuli. Figure 4a illustrates the working principle of synaptic memory. For STP operation, we apply an electrochemical (EC) pulse (pulse width = 500 ms) <2 V between the ion gel and MoS₂ through the top gold electrode. The conductivity of the synaptic device rises from 10⁻⁵ to 10⁻¹ mS when the bias is applied (EC pulse ON), reaching a high-conductance state; when the bias is removed (EC pulse OFF), the conductivity drops immediately back to the original low conductance state. As revealed in the plot in Figure 4b, the STP is triggered when a voltage exceeding 0.5 V is applied with an output STP signal being proportional to the EC input. Conversely, LTP is attained when an EC input exceeds +2 V. Successive LTP EC input mediates an accumulative number of Fc⁺ molecules adsorbed on MoS₂, changing the magnitude of the memorized conductivity of MoS₂ at each pulse. We define 4 major memory states that represent different magnitudes of conductivity triggered by the EC stimulus: low-conductance state, mid-low conductance state, mid-high conductance state, and high conductance state. The difference between each state is distinct with the highest and lowest conductance ratio reaching 10⁶. Each memory state can sustain long-term stability (Figure S11, Supporting Information). The major states could be regulated by stimulating the synapse with continuous EC pulses during the potentiation and depression process (Figure 4c). Potentiation is found to be efficient and reaching saturation with 6 pulses at +2.5 V. However, for depression, a greater amount (>200) of EC pulses at -5 V is needed to decrease the conductance from the high to the low conductance state. The synaptic process performs excellent paired-pulse facilitation, which is evaluated and discussed in Figure S12 (Supporting Information). For our Janus MoS₂, the asymmetric functions do not couple with each other, enabling independent yet collective properties modulation of the current output upon using the different stimuli. Such characteristics make it possible to enrich each electrochemically-established major state with optically driven sub-states featuring small conductance differences (Figure 4a). Figure 4d portrays the ultimate outcome in an opto-electrochemical synaptic device. At each major state, optical memory can be encoded with 4s pulses

of UV light. At least 16 sub-states can be established at each memory state. These finely-tuned potentiation states can be fully recovered by the depression process triggered by the reduction of Fc/Fc⁺, given that the electrochemical reduction of the pairs shows a much smaller conductivity gap between each stimulus. We have observed that at a high conductance state the optical stimulus does not function because of the high degree of coverage of Fc⁺ on the top surface of MoS₂ filtering out the photons which therefore do not reach the Azo molecules placed underneath the 2D semiconductor. By exploiting the binary stimulus, a 4-bit memory can be established within a single synaptic device, boosting the efficiency in neuromorphic computing when compared to traditional 2-bit manipulation in 2D semiconductors. Furthermore, the Janus functionalized 2D MoS₂ devices can be highly reproducible and robust against cycles, which is appealing for scalable fabrication applications (Figures S13–S16, Supporting Information).

3. Conclusion

In summary, we demonstrated that the asymmetric dressing of the two faces of 2D MoS₂ can be employed to introduce the required functionalities to emulate artificial synapses, triggered by opto-electrochemical stimuli. Such asymmetric functionalization leads to a Janus Fc/MoS₂/Azo structure which is capable of mimicking STP and multi-level LTP and depression up to 4-bits (16 states) logic in a single device. We carefully analyzed the mechanism of current modulation by electrochemical redox switching of the top Fc/Fc⁺ layer, finding that a transition between STP and LTP occurs at input signal exceeding 2.0 V. Sub-states of LTP can be encoded through the optical switching of azobenzene that is self-assembled on the Au substrate and is interfacing the bottom surface of 2D materials. The Azo isomerization and associated conformational photochemical isomerization between the *trans* and the *cis* state modulate the doping of 2D MoS₂, thereby influencing the intra-sheet conductivity. Compared to literature reports, our bi-responsive, Janus 2D semiconductor stands out representing an ideal hybrid system for the fabrication of artificial synapse which integrates in a single device complex functions which can be programmed by exploiting the large versatility of organic molecular switches to boost the performance in elementary devices for high-performance electronics (Table S1, Supporting Information).

4. Experimental Section

Device Fabrication: Device fabrication was initiated by patterning the bottom electrodes with photolithography (laser writer LW405B from Microtech, AZ1505 photoresist) on thermally oxidized heavily n-doped silicon substrates (Fraunhofer Institute IPMS, $\rho_{Si} \approx 0.001 \Omega \text{ cm}$, $t_{ox} = 270 \text{ nm}$) followed by metal deposition (0.5 nm Cr / 30 nm Au) and lift-off process. The azobenzene (Azo) SAM was grown on the bottom electrode by immersing the substrate with a gold electrode in 0.1 mM of Azo solution in chloroform for 48 h in a dark environment. After rinsing with chloroform and blow-dry with a nitrogen gun to remove the excess physisorbed molecules, few-layer MoS₂ flakes were mechanically exfoliated from bulk crystals (Furuchi, Japan) and dry-transferred on the functionalized bottom electrode using polydimethylsiloxane (PDMS) (Gel-Pak). The thickness of the flakes was monitored by an optical microscope combined with Raman spectroscopy and AFM. A top electrode

was subsequently patterned using a laser writer followed by deposition of 50 nm Au. The devices were thermally annealed at 150 °C inside a vacuum chamber to desorb atmospheric adsorbates. The top ion-gel was prepared by mixing Diethylmethyl(2-methoxyethyl)ammonium bis(trifluoromethylsulfonyl)imide (DEME-TFSI, Merck), Poly(vinylidene fluoride-co-hexafluoropropylene) (PVDF-HFP, Merck) and acetone with a weight ratio of 4:1:7. The mixture was stirred at room temperature for 5 h. Different amount of ferrocene (1, 2, and 5 mg) was subsequently added and stir-mixed with 1 mL of the mother ion gel. One microlitre of the mixture was drop-casted onto the device to completely cover the MoS₂ flake and the side gate electrode on a hotplate at 50 °C in an N₂-filled glovebox.

Electrical Characterizations: The characterization of device performance was realized by Keithley 2636A and 2635A under N₂ atmosphere. The in situ photoswitching was performed by a Polychrome V system (Thermo Fisher) used as the monochromatic light source. The output power was calibrated by a PM100A Power Meter (Thorlabs) where the 365 nm UV light was 9.69 mW cm⁻² and 455 nm Vis light was 23.88 mW cm⁻². All the electrical measurements were done in the dark to exclude the photoconductive effect of 2D materials.

Raman Spectroscopy: Raman and photoluminescence spectra were carried out by Renishaw inVia a spectrometer equipped with a 532 nm laser. The excitation power was kept below 1 mW to avoid local heating damage effects. The wavenumber (energy) resolution was ≈ 1 meV.

AFM Measurement: AFM imaging was performed by means of a Bruker Dimension Icon set-up operating in air, in tapping mode, by using tip model TESPA-V2 (tip stiffness: $k = 42 \text{ N m}^{-1}$).

Supporting Information

Supporting Information is available from the Wiley Online Library or from the author.

Acknowledgements

The authors thank Prof. Yifan Yao (Hunan University, P.R.China) for valuable discussions. The authors also acknowledge funding from the European Commission through the ERC project SUPRA2DMAT (GA-833707), the Graphene Flagship Core 3 project (GA-881603) as well as the Agence Nationale de la Recherche through the Interdisciplinary Thematic Institute SysChem via the IdEx Unistra (ANR-10-IDEX-0002) within the program Investissement d'Avenir, the International Center for Frontier Research in Chemistry (icFRC) and the Institut Universitaire de France (IUF).

Conflict of Interest

The authors declare no conflict of interest.

Author Contributions

P.S. and Y.W. conceived and coordinated the work. Y.W. worked on sample preparation, device fabrication, and optical and electrical characterization. B.H. carried out XPS measurements. M.M. synthesized the azobenzene. Y.W. analyzed the data. Y.W. and P.S. wrote the paper with all the authors contributing to the discussion and preparation of the manuscript.

Data Availability Statement

The data that support the findings of this study are available from the corresponding author upon reasonable request.

Keywords

2D materials, memories, molecular switches, synapses, transition metal dichalcogenides

Received: July 24, 2023
Revised: October 25, 2023
Published online:

- [1] a) J. C. Magee, C. Grienberger, *Annu. Rev. Neurosci.* **2020**, *43*, 95; b) A. Gumyusenge, A. Melianas, S. T. Keene, A. Salleo, *Annu. Rev. Mater. Res.* **2021**, *51*, 47; c) K. Zhu, S. Pazos, F. Aguirre, Y. Shen, Y. Yuan, W. Zheng, O. Alharbi, M. A. Villena, B. Fang, X. Li, *Nature* **2023**, *618*, 57; d) M. Lanza, F. Hui, C. Wen, A. C. Ferrari, *Adv. Mater.* **2023**, *35*, 2205402; e) S. T. Keene, C. Lubrano, S. Kazemzadeh, A. Melianas, Y. Tuchman, G. Polino, P. Scognamiglio, L. Cinà, A. Salleo, Y. van de Burgt, *Nat. Mater.* **2020**, *19*, 969.
- [2] G. Lee, J. H. Baek, F. Ren, S. J. Pearton, G. H. Lee, J. Kim, *Small* **2021**, *17*, 2100640.
- [3] G. Cao, P. Meng, J. Chen, H. Liu, R. Bian, C. Zhu, F. Liu, Z. Liu, *Adv. Funct. Mater.* **2021**, *31*, 2005443.
- [4] S. Bertolazzi, P. Bondavalli, S. Roche, T. San, S. Y. Choi, L. Colombo, F. Bonaccorso, P. Samorì, *Adv. Mater.* **2019**, *31*, 1806663.
- [5] M. Gobbi, E. Orgiu, P. Samorì, *Adv. Mater.* **2018**, *30*, 1706103.
- [6] T. F. Schranghamer, A. Oberoi, S. Das, *Nat. Commun.* **2020**, *11*, 5474.
- [7] a) M. Lanza, A. Sebastian, W. D. Lu, M. Le Gallo, M.-F. Chang, D. Akinwande, F. M. Puglisi, H. N. Alshareef, M. Liu, J. B. Roldan, *Science* **2022**, *376*, eabj9979; b) Y. Shi, X. Liang, B. Yuan, V. Chen, H. Li, F. Hui, Z. Yu, F. Yuan, E. Pop, H.-S. P. Wong, *Nat. Electron.* **2018**, *1*, 458.
- [8] V. K. Sangwan, H.-S. Lee, H. Bergeron, I. Balla, M. E. Beck, K.-S. Chen, M. C. Hersam, *Nature* **2018**, *554*, 500.
- [9] Y. Zhao, M. Gobbi, L. E. Hueso, P. Samorì, *Chem. Rev.* **2021**, *122*, 50.
- [10] a) R. Xu, H. Jang, M.-H. Lee, D. Amanov, Y. Cho, H. Kim, S. Park, H. Shin, D. Ham, *Nano Lett.* **2019**, *19*, 2411; b) A. Krishnaprasad, D. Dev, S. S. Han, Y. Shen, H.-S. Chung, T.-S. Bae, C. Yoo, Y. Jung, M. Lanza, T. Roy, *ACS Nano* **2022**, *16*, 2866; c) M. Huang, W. Ali, L. Yang, J. Huang, C. Yao, Y. Xie, R. Sun, C. Zhu, Y. Tan, X. Liu, *Adv. Sci.* **2023**, *10*, 2300120; d) N. Mohta, A. Rao, N. Remesh, R. Muralidharan, D. N. Nath, *RSC Adv.* **2021**, *11*, 36901; e) J. Yu, X. Yang, G. Gao, Y. Xiong, Y. Wang, J. Han, Y. Chen, H. Zhang, Q. Sun, Z. L. Wang, *Sci. Adv.* **2021**, *7*, eabd9117.
- [11] V. Montes-García, P. Samorì, *Chem. Sci.* **2022**, *13*, 315.
- [12] G. Pace, V. Ferri, C. Grave, M. Elbing, C. von Hänisch, M. Zharnikov, M. Mayor, M. A. Rampi, P. Samorì, *Proc. Natl. Acad. Sci. U. S. A.* **2007**, *104*, 9937.
- [13] D. J. Late, B. Liu, H. R. Matte, V. P. Dravid, C. Rao, *ACS Nano* **2012**, *6*, 5635.
- [14] a) Y. Choi, J. Kang, D. Jariwala, M. S. Kang, T. J. Marks, M. C. Hersam, J. H. Cho, *Adv. Mater.* **2016**, *28*, 3742; b) J. Pu, Y. Yomogida, K.-K. Liu, L.-J. Li, Y. Iwasa, T. Takenobu, *Nano Lett.* **2012**, *12*, 4013; c) J. H. Cho, J. Lee, Y. Xia, B. Kim, Y. He, M. J. Renn, T. P. Lodge, C. Daniel Frisbie, *Nat. Mater.* **2008**, *7*, 900; d) H. Kim, D.-H. Lien, M. Amani, J. W. Ager, A. Javey, *ACS Nano* **2017**, *11*, 5179.
- [15] D. Bao, B. Millare, W. Xia, B. G. Steyer, A. A. Gerasimenko, A. Ferreira, A. Contreras, V. I. Vullev, *J. Phys. Chem. A* **2009**, *113*, 1259.
- [16] a) T. Leydecker, M. Herder, E. Pavlica, G. Bratina, S. Hecht, E. Orgiu, P. Samorì, *Nat. Nanotechnol.* **2016**, *11*, 769; b) H. Qiu, M. Herder, S. Hecht, P. Samorì, *Adv. Funct. Mater.* **2021**, *31*, 2102721.
- [17] N. Crivillers, A. Liscio, F. Di Stasio, C. Van Dyck, S. Osella, D. Cornil, S. Mian, G. Lazzerini, O. Fenwick, E. Orgiu, *Phys. Chem. Chem. Phys.* **2011**, *13*, 14302.
- [18] N. Crivillers, E. Orgiu, F. Reinders, M. Mayor, P. Samorì, *Adv. Mater.* **2011**, *23*, 1447.
- [19] a) S. Bertolazzi, M. Gobbi, Y. Zhao, C. Backes, P. Samorì, *Chem. Soc. Rev.* **2018**, *47*, 6845; b) Y. Wang, S. M. Gali, A. Slassi, D. Beljonne, P. Samorì, *Adv. Funct. Mater.* **2020**, *30*, 2002846.

- [20] Y. Wang, D. Iglesias, S. M. Gali, D. Beljonne, P. Samorì, *ACS Nano* **2021**, *15*, 13732.
- [21] M. Gobbi, S. Bonacchi, J. X. Lian, A. Vercouter, S. Bertolazzi, B. Zyska, M. Timpel, R. Tatti, Y. Olivier, S. Hecht, *Nat. Commun.* **2018**, *9*, 2661.
- [22] C. S. Lau, J. Y. Chee, Y. S. Ang, S. W. Tong, L. Cao, Z.-E. Ooi, T. Wang, L. K. Ang, Y. Wang, M. Chhowalla, *ACS Nano* **2020**, *14*, 13700.
- [23] M. Elbing, A. Błaszczuk, C. von Hänisch, M. Mayor, V. Ferri, C. Grave, M. A. Rampi, G. Pace, P. Samorì, A. Shaporenko, *Adv. Funct. Mater.* **2008**, *18*, 2972.